

Bayesian uncertainty quantification in linear models for diffusion MRI

Jens Sjölund^{*1, 2, 3}, Anders Eklund^{1, 2, 4}, Evren Özarslan^{1, 2},
Magnus Herberthson⁵, Maria Bånkestad⁶ and Hans Knutsson^{1,2}

¹*Department of Biomedical Engineering, Linköping University, Linköping, Sweden*

²*Center for Medical Image Science and Visualization (CMIV), Linköping University, Linköping, Sweden*

³*Elekta Instrument AB, Kungstensgatan 18, Box 7593, SE-103 93 Stockholm, Sweden*

⁴*Department of Computer and Information Science, Linköping University, Linköping, Sweden*

⁵*Department of Mathematics, Linköping University, Linköping, Sweden*

⁶*RISE SICS, Isafjordsgatan 22, Box 1263, SE-164 29 Kista, Sweden*

April 25, 2022

Abstract

Diffusion MRI (dMRI) is a valuable tool in the assessment of tissue microstructure. By fitting a model to the dMRI signal it is possible to derive various quantitative features and to perform white matter tractography. Several of the most popular dMRI signal models are expansions in an appropriately chosen basis, where the coefficients are determined using some variation of least-squares. However, such approaches lack any notion of uncertainty, which could be valuable in e.g. group analyses or tractography. In this work, we use a probabilistic interpretation of linear least-squares methods to recast popular dMRI models as Bayesian ones. This makes it possible to quantify the uncertainty of any derived quantity. In particular, for quantities that are affine functions of the coefficients, the posterior distribution can be expressed in closed-form. We simulated measurements from single- and double-tensor models where the correct values of several quantities are known, to validate that the theoretically derived quantiles agree with those observed empirically. The validation employed several different models: Diffusion Tensor Imaging (DTI), Mean Apparent Propagator MRI (MAP-MRI) and Constrained Spherical Deconvolution (CSD). We also used data from the Human Connectome Project to demonstrate the uncertainty quantification in vivo. In summary, we convert successful linear models for dMRI signal estimation to probabilistic models, capable of accurate uncertainty quantification.

Keywords— Diffusion MRI, uncertainty quantification, signal estimation

*Corresponding author. E-mail address: jens.sjolund@liu.se

1 Introduction

Diffusion magnetic resonance imaging (dMRI) permits the noninvasive assessment of tissue microstructure. By fitting a model of the dMRI signal in each voxel it is possible to trace virtual “fibers” — a procedure referred to as (computational) tractography. The rationale for tractography is that connectivity patterns define functional networks, allowing neuroscientists to infer function from structure [24]. Diffusion MRI can also be used to derive various quantitative features. Examples include voxel-based scalar indices such as fractional anisotropy (FA) or return to origin probability (RTOP), as well as the pairwise probability of a pathway being traced between two points. Using such measures it is possible to perform statistical group analyses. For the reliability of such tests it is essential to quantify the uncertainty of the relevant measures. This fact is well-established in the field of functional magnetic resonance imaging (fMRI) — where it is common to, for example, downweight subjects with a high variance [9, 49] — but not so for dMRI; the most popular approach for doing FA group comparisons [39] ignores uncertainty in FA.

A large body of research has been devoted to formulating new diffusion models that address the inability of diffusion tensor imaging (DTI) [4] to resolve crossing and kissing fibers. A common trait among several of the most widely used methods is that they expand the signal in an appropriately chosen functional basis. Often, the coefficients of the expansion are then determined by some variation of linear least-squares (see Table 1 for a non-exhaustive list). This is precisely the type of models we are concerned with in this paper — linear (in the coefficients) models fitted with least-squares. Incidentally, some non-parametric models [1, 38] also belong to this class, although we will not elaborate on the connection here. Our key observation is that linear models fitted with least-squares are amenable to a probabilistic reinterpretation. We will show that it follows almost immediately that, under the same assumptions as in the fitting, it is possible to determine the full posterior distribution of the coefficients — not just a point estimate.

This is, of course, not the first time someone has taken a probabilistic view on signal estimation in dMRI. It is well-known that the noisy signal in MRI follows a Rician, or more generally a non-central Chi, distribution [19], which on the other hand is approximately Gaussian when the signal-to-noise ratio is, at least, moderately high ($\gtrsim 3$). In DTI [4] and diffusion kurtosis imaging (DKI) [22], it is common to fit a linear model to the logarithm of the signal. The resulting log-Rician distribution is again approximately normal for moderate signal-to-noise ratios, but with signal-dependent (heteroscedastic) noise [36]. In such cases, weighted least-squares has been shown to work well [34, 44]. Error propagation in DTI fitted with nonlinear least-squares has also been investigated [28].

Bayesian methods [6, 16, 18, 45] are distinctly different from methods using least-squares to find point estimates. By assuming parametric probability distributions for the likelihood and for every parameter in the model, Bayesian methods make it possible to derive the probability distribution of any quantity of interest, at least in principle. Actually evaluating such distributions, however,

typically relies extensively on sampling methods such as Markov Chain Monte Carlo.

Bootstrapping is a frequentistic alternative to Bayesian models. The general idea is to approximate the underlying probability distribution with an empirical one. Samples are drawn with replacement and for each draw the parameter of interest is calculated. By repeating this procedure, it is possible to approximate the sampling distribution of the relevant parameter. Naturally, the quality of the approximation degrades as the number of empirical samples decreases. Residual bootstrap [10] and wild bootstrap [47] are two forms of model-based bootstrapping that have been applied to dMRI. In residual bootstrap, the normalized residuals (after fitting a model) are resampled, and the fitting procedure is repeated for this new draw, after which the parameter value of interest is recorded. All residuals are assumed to have identical distributions and resampling is done freely among them. In wild bootstrap, on the other hand, modified residuals are randomly added or subtracted to the fitted point where they originated from, without being distributed to other design points. Model-based bootstrapping is only reliable insofar as the model can adequately describe the measured diffusion signals [50].

In tractography, the propagation of errors has a clear risk of leading to erroneous reconstructions of pathways. Quantifying the uncertainty is thus of particular relevance. This is shown, if nothing else, by the fact that basically all of the methods described above have been applied to tractography [5, 20, 23, 25, 26].

In this work, instead of starting out by assuming more or less contrived prior distributions for the coefficients and the likelihood, we look at methods that are tried and tested and see what the corresponding priors are. Surprisingly, it results in a simple closed form expression for the posterior distribution of coefficients, and by extension also of all parameters linear in the coefficients. In other cases, such as tractography, there is no need to repeat the whole fitting procedure, as in bootstrapping methods. Since the posterior is available in closed form it is very efficient to sample from it directly.

2 Theory

To recapitulate, we focus on linear models fitted with linear least-squares. This might sound restrictive at first but — as can be seen in Table 1 — it encompasses several of the most widely used models in dMRI. A broad distinction can be made between those derived from a cumulant expansion of the signal [4, 36, 44, 46] and those where the signal is expanded in a, typically orthogonal, basis [3, 8, 11, 12, 13, 21, 31, 41, 42].

Method	y	$\phi(\mathbf{x})$	\mathbf{c}	W	Λ
Diffusion Tensor Imaging (DTI) (weighted least-squares) [4, 36]	$\log S(\mathbf{q})$	$1, q_i q_j$	$\log S_0, D_{ij}$	$\text{diag}(S^2)$	0
Diffusion Kurtosis Imaging (DKI) (weighted least-squares) [44]	$\log S(\mathbf{q})$	$1, q_i q_j, q_i q_j q_k q_l$	$\log S_0, D_{ij}, K_{ijkl}$	$\text{diag}(S^2)$	0
Q-space Trajectory Imaging (QTI) [46]	$\log S(B)$	$1, B, B^{\otimes 2}$	$\log S_0, \langle D \rangle, \mathbb{C}$	$\text{diag}(S^2)$	0
Constrained Spherical Deconvolution (CSD)[41]	$S(\hat{\mathbf{q}})$	$\chi(\hat{\mathbf{q}})Y_l(\hat{\mathbf{q}})$	c_l	I	L
Q-Ball Imaging (QBI) [12, 42]	$S(\hat{\mathbf{q}})$	$Y_l(\hat{\mathbf{q}})$	c_l	I	$\int_{S^2} \ \Delta_b S\ ^2 d\Omega$
MAP-MRI with Laplacian regularization (MAPL) [13, 31]	$S(\mathbf{q})$	$\Phi_n(u, q)$	c_n	I	$\int_{\mathbb{R}^3} \ \Delta S\ ^2 d\mathbf{q}$
Spherical Polar Fourier (SPF) [3]	$S(\mathbf{q})$	$R_k(q)Y_l(\hat{\mathbf{q}})$	c_{kl}	I	$\Lambda_R + \Lambda_Y$

- y : response variable
- \mathbf{x} : input variables
- $\phi(\mathbf{x})$: basis function
- \mathbf{c} : coefficients
- W : inverse noise correlation matrix
- Λ : regularization matrix
- S : signal
- S_0 : non-diffusion weighted signal
- χ : single fiber response function
- Y_l : real spherical harmonics, cf. [12]
- L : matrix determined iteratively using a sparsifying heuristic
- Δ : Laplace operator
- Δ_b : Laplace-Beltrami operator
- Φ_n : Hermite functions scaled by a factor u
- R_k : Gaussian Laguerre polynomials
- Λ_R : diagonal matrix penalizing higher radial orders
- Λ_Y : diagonal matrix penalizing higher angular orders

Table 1: An assortment of linear models used in dMRI. We have used the notation $\mathbf{q} = q \hat{\mathbf{q}}$ where applicable. For clarity, some details have been omitted.

Differences aside, all these models assume that, in the absence of noise, it would hold that

$$\mathbf{y}(\mathbf{x}) = \sum_{i=1}^d c_i \phi_i(\mathbf{x}), \quad (1)$$

where y is the response variable that we want to model, \mathbf{x} defines a measurement and $\phi_i(\mathbf{x})$ are (possibly nonlinear) functions with corresponding coefficients c_i . In a typical scenario, we are given n observations (\mathbf{x}_j, y_j) and the objective is to determine an estimate $\hat{\mathbf{c}}$ such that $\mathbf{y} \approx \Phi \hat{\mathbf{c}}$, where we have introduced the matrix $\Phi_{ji} = \phi_i(\mathbf{x}_j)$. Most of the works cited in Table 1 simply state their estimate in one of these forms:

$$\hat{\mathbf{c}} = \begin{cases} (\Phi^T \Phi)^{-1} \Phi^T \mathbf{y} & \text{(ordinary least-squares)} \\ (\Phi^T W \Phi)^{-1} \Phi^T W \mathbf{y} & \text{(weighted least-squares)} \\ (\Phi^T \Phi + \Lambda)^{-1} \Phi^T \mathbf{y} & \text{(Tikhonov regularization)}. \end{cases} \quad (2)$$

These are all special cases of the estimate

$$\hat{\mathbf{c}} = (\Phi^T W \Phi + \Lambda)^{-1} \Phi^T W \mathbf{y}, \quad (3)$$

but what is the probabilistic interpretation? In the next section, we show that equation (3) arises naturally as the maximum-a-posteriori solution of a Bayesian linear regression problem.

2.1 Least-squares and Bayesian linear regression

Suppose that the observations are given by adding Gaussian noise $\boldsymbol{\epsilon}$ to the model in equation (1),

$$\mathbf{y}(\mathbf{x}) = \Phi \mathbf{c} + \boldsymbol{\epsilon}, \quad \boldsymbol{\epsilon} \sim \mathcal{N}(0, \sigma^2 W^{-1}). \quad (4)$$

We assume that the matrix W , determining the structure of the noise, is known but not the scale σ^2 . It follows that the likelihood — the probability distribution of the observations given the parameters — is

$$p(\mathbf{y}|\mathbf{c}, \mathbf{x}) = \mathcal{N}(\Phi \mathbf{c}, \sigma^2 W^{-1}). \quad (5)$$

As is typical in the Bayesian formalism, we may specify a prior probability density over the coefficients \mathbf{c} . Suppose that we use

$$p(\mathbf{c}) = \mathcal{N}(0, \sigma^2 \Lambda^{-1}), \quad (6)$$

where Λ is known. We may assume that the expected value $\mu_{\mathbf{c}}$ is zero without loss of generality, since it is always possible to subtract $\Phi \mu_{\mathbf{c}}$ from the response variable. Bayes' rule then gives the posterior — the probability distribution of the coefficients given the data — as follows

$$p(\mathbf{c}|\mathbf{y}, \mathbf{x}) = \frac{p(\mathbf{y}|\mathbf{c}, \mathbf{x})p(\mathbf{c})}{p(\mathbf{y}|\mathbf{x})}. \quad (7)$$

Inserting the expressions for the likelihood and prior from above, it is a straightforward exercise in probability theory [7] to show that the posterior distribution is again a normal distribution, given by

$$\begin{aligned} p(\mathbf{c}|\mathbf{y}, \mathbf{x}) &= \mathcal{N}(\boldsymbol{\mu}, \Sigma), \\ \boldsymbol{\mu} &= Q^{-1}\Phi^T W \mathbf{y}, \\ \Sigma &= \sigma^2 Q^{-1}, \end{aligned} \tag{8}$$

where $Q = \Phi^T W \Phi + \Lambda$. We recognize that the least-squares estimate (3) is the mean of the posterior distribution (8), which for a Gaussian distribution is the same as the maximum-a-posterior solution. However, what this line of reasoning also gives you — almost for free — is a quantification of the uncertainty in the prediction. The only unknown variable that we need to estimate is the residual variance, σ^2 .

2.2 Residual variance

We will start with the residual variance estimate for ordinary least-squares and then generalize it in two steps. The first step is to consider regularized least-squares under white noise. The second step is to reduce weighted least-squares to ordinary least-squares using a transformation of variables. Combining these two steps we will arrive at a unified expression.

For an ordinary linear regression model with n observations and d basis functions, the residual variance is estimated as

$$\hat{\sigma}^2 = \frac{\|\mathbf{y} - \hat{\mathbf{y}}\|^2}{\nu}, \tag{9}$$

where $\nu = n - d$ is referred to as the degrees of freedom. To generalize to regularized least-squares, we introduce the smoother matrix H , such that $\hat{\mathbf{y}} = \Phi \hat{\mathbf{c}} = H \mathbf{y}$ [14]. Then, assuming white noise ($W = I$), the degrees of freedom for regularized least-squares can be written as [30, 34]

$$\nu = \|I - H\|_{\text{Fro}}^2 = n - \text{Tr}(2H - H^T H). \tag{10}$$

Note that when $\Lambda = 0$ it holds that $H^T H = H$ and $\text{Tr}(H) = d$, in which case the expression reduces to the one for ordinary least-squares, as expected.

The colored noise case ($W \neq I$) can be handled by a whitening transformation. Using for instance the Cholesky decomposition $L^T L = W$ and left-multiplying equation (4) with L transforms it into

$$\tilde{\mathbf{y}} = \tilde{\Phi} \mathbf{c} + \tilde{\epsilon}, \quad \tilde{\epsilon} \sim \mathcal{N}(0, \sigma^2 I), \tag{11}$$

where we have used a tilde to denote transformed variables, i.e. $\tilde{\mathbf{y}} = L \mathbf{y}$, $\tilde{\Phi} = L \Phi$ and $\tilde{\epsilon} = L \epsilon$. One can then proceed as in the white noise case.

This brings us to a unified expression for the estimate of residual variance

$$\hat{\sigma}^2 = \frac{\left\| (I - \tilde{H}) \tilde{\mathbf{y}} \right\|_2^2}{\left\| I - \tilde{H} \right\|_{\text{Fro}}^2} = \frac{\|L(\mathbf{y} - \hat{\mathbf{y}})\|_2^2}{\|I - LHL^{-1}\|_{\text{Fro}}^2}, \quad (12)$$

where $\tilde{H} = L\Phi(\Phi^T W\Phi + \Lambda)^{-1}\Phi^T L^T = LHL^{-1}$.

2.3 Uncertainty of the residual variance estimate

It would be possible to insert the point estimate (12) of the residual variance in equation (8) to get a closed-form expression for the posterior distribution. However, this neglects the uncertainty in the residual variance estimation. We can handle this uncertainty in a Bayesian way, by specifying a distribution over the variance σ^2 . We then determine the posterior distribution for the coefficients by integrating over $p(\sigma^2)$; this procedure is referred to as marginalization.

In appendix A we show that there is a particularly convenient prior (inverse-Gamma distribution) for which the posterior is a multivariate t -distribution [29, 35],

$$p(\mathbf{c}|\mathbf{y}, \mathbf{x}) = t_\nu(\boldsymbol{\mu}, R), \quad (13)$$

where the mean $\boldsymbol{\mu}$, the degrees of freedom ν and the correlation matrix R are given by

$$\begin{aligned} \boldsymbol{\mu} &= Q^{-1}\Phi^T W\mathbf{y}, \\ \nu &= \|I - H\|_{\text{Fro}}^2, \\ R &= \frac{\nu - 2}{\nu} \hat{\sigma}^2 Q^{-1}. \end{aligned} \quad (14)$$

We emphasize that this replaces equation (8) as the main expression for the uncertainty in the coefficients. Note that the mean, covariance and degrees of freedom are the same as before, but the t -distribution has fatter tails than the Gaussian distribution, reflecting the uncertainty in the variance. As the degrees of freedom increases it becomes more similar to a Gaussian distribution; a rule of thumb is that for $\nu \gtrsim 30$ the t -distribution can be replaced by a Gaussian.

2.4 Corollaries

We can imagine a multitude of uses for the posterior distribution (13).

- The multivariate t -distribution is closed under affine transformations [35], which means any property $\boldsymbol{\theta} = A\mathbf{c} + \mathbf{b}$ also follows a multivariate t -distribution, namely

$$\boldsymbol{\theta} \sim t_\nu(A\boldsymbol{\mu} + \mathbf{b}, ARA^T). \quad (15)$$

This makes it possible to, for instance, compute credible intervals (confidence intervals).

- The distribution of a property $\theta = f(\mathbf{c})$, nonlinearly dependent on the coefficients, can be determined analytically in some cases, notably if f is invertible. Regardless, it is always possible to estimate the distribution by sampling from the posterior.
- If the coefficients are used to condition a probability distribution $p(\theta|\mathbf{c})$, for instance when sampling fiber orientation in probabilistic tractography, one can, at least formally, write down the expression for the posterior predictive distribution:

$$p(\theta|\mathbf{y}, \mathbf{x}) = \int p(\theta|\mathbf{c})p(\mathbf{c}|\mathbf{y}, \mathbf{x})d\mathbf{c}. \quad (16)$$

2.5 Evaluation

We base most of our quantitative evaluation on the seemingly self-evident statement that “in p % of the cases the correct value should be smaller than the p th quantile”. To formalize this statement, recall the definition of the cumulative distribution function of a random variable X : $F_X(x) = \Pr(X \leq x)$. The quantile function Q is, under mild assumptions, the inverse cumulative distribution function, $Q = F^{-1}$. Stated differently, the quantile function specifies, for a given probability p , the value x at which the probability of the random variable is less than or equal to the given probability, $\Pr(X \leq x) = p$.

In our case, given a measurement \mathbf{y}_j we get a posterior distribution of the quantity of interest θ_j following the line of reasoning presented in the previous sections. For a fixed probability p the corresponding quantile, $q_j = Q_j(p)$, can be estimated. If we know the correct value θ^* , we can observe empirically how often $\theta^* \leq q_i$, and compare this with the theoretically expected probability p . This procedure can be repeated for a range of probabilities p , after which the comparison can be presented graphically in a so called P-P (probability-probability) plot [48].

We also use the interquartile range (*IQR*) to summarize the dispersion in a single number. The interquartile range is defined as the difference between the third and the first quartile, i.e. $IQR = Q(0.75) - Q(0.25)$. For a symmetric distribution it would thus correspond to the 50% confidence interval. One of its main advantages is that it is more robust to outliers than, for instance, the standard deviation.

3 Results

We implemented the core algorithmic ideas by extending the free and open source software project Dipy (Diffusion Imaging in Python) [15]. The code for our modified version of Dipy is available online¹. We made a quantitative analysis of the proposed method on simulated data, and a qualitative analysis on in vivo data from the Human Connectome Project [43].

¹<https://github.com/jsjol/dipy>

3.1 Simulated data

We simulated data from single- and double-tensor models. For these models, we can calculate the correct values of several quantities analytically.

In the single-tensor case the mean diffusivity (MD) and fractional anisotropy (FA) are given, respectively, by

$$MD = \frac{\text{Tr}(D)}{3}, \quad (17)$$

$$FA = \sqrt{\frac{1}{2} \left(3 - \frac{\text{Tr}(D)^2}{\text{Tr}(D^2)} \right)}, \quad (18)$$

where D is the diffusion tensor in question. The above, non-standard, expression for FA elucidates its nonlinear dependence on D [32].

In the double-tensor case, the crossing angle is known by design and can be compared with those returned by peak detection algorithms. In addition, there are some scalar indices that can be calculated analytically [31], e.g. the return to origin probability (RTOP)

$$RTOP = \frac{1}{S_0} \int_{\mathbb{R}^3} S(\mathbf{q}) d\mathbf{q}. \quad (19)$$

3.1.1 Single tensor model

We simulated a signal from a Gaussian distribution with diffusion tensor $D = D_0 \cdot \text{diag}(1, 0.2, 0.2)$ where $D_0 = 1.5 \cdot 10^{-3} \text{ mm}^2/\text{s}$. The resulting mean diffusivity is $0.7 \cdot 10^{-3} \text{ mm}^2/\text{s}$ and the fractional anisotropy is 0.77. This is roughly equivalent to a white matter tract [33]. Assuming a Stejskal-Tanner type measurement [40], the latent signal was

$$S(\mathbf{q}) = S_0 e^{-4\pi^2 t_d \mathbf{q}^T D \mathbf{q}}, \quad (20)$$

where $t_d = \Delta - \delta/3$; here Δ is the mixing time and δ the pulse duration. We used the same experimental parameters as in the Human Connectome data described in section 3.2, but with maximum b -value ($b = 4\pi^2 t_d q^2$) equal to $1000 \text{ s}/\text{mm}^2$.

Based on the latent signal, we simulated 1000 independent measurements following a Rician distribution with scale $\sigma = 0.05 S_0$. For each measurement we used weighted least-squares to fit a diffusion tensor model. The coefficients in the fitting thus include D_{xx} , D_{yy} and D_{zz} . Recalling the definition of mean diffusivity (18), we see that it is a linear function of the coefficients. Using equation (15) we find that the posterior distribution follows a univariate t -distribution. The P-P plot in Figure 1a shows the frequency with which the quantiles based on noisy measurements contain the correct value of the mean diffusivity.

Fractional anisotropy, on the other hand, is a nonlinear function of the coefficients, which means that we have to resort to sampling to estimate its posterior distribution. For each measurement the quantiles were estimated from 1000

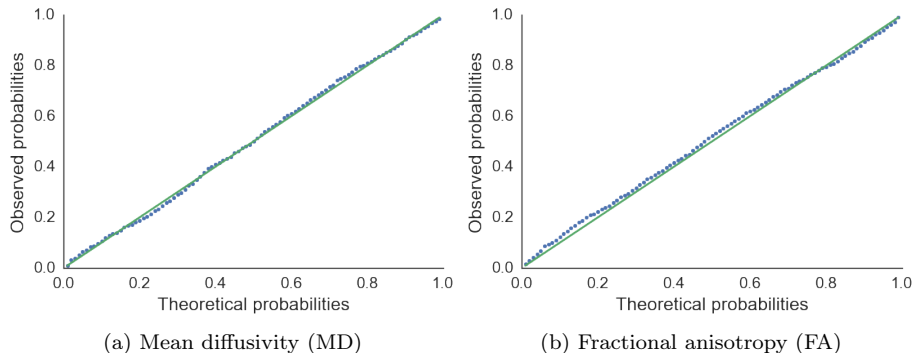


Figure 1: P-P plots of mean diffusivity (MD) and fractional anisotropy (FA) for 1000 simulated measurements from a single tensor model. The properties, MD and FA, were estimated using a DTI model fitted with weighted least-squares. Averaging over the simulations, the P-P plots show how often the correct value is smaller than the quantiles corresponding to the theoretically expected probabilities for that property given a simulated measurement.

samples from the posterior of the coefficients. The resulting P-P plot is shown in Figure 1b.

3.1.2 Double tensor model

We defined the double tensor signal as the sum of two, equal magnitude, single tensor signals as in the previous section, but where the second was rotated by 60° about the y -axis. Again, we used the same experimental parameters as in the Human Connectome data described in section 3.2, but this time with maximum b -value equal to 3000 s/mm^2 . Based on the double tensor signal, we simulated 1000 independent measurements following a Rician distribution with scale $\sigma = 0.05 S_0$.

The return to origin probability (RTOP) for a multi tensor model with equal diffusion tensors is the same as for a single tensor model, namely

$$RTOP = \det(4\pi t_d D)^{-1/2}, \quad (21)$$

which in this case evaluates to $0.83 \cdot 10^6 \text{ mm}^{-3}$.

For each measurement we fitted a MAP-MRI model [31] with a Laplacian regularization determined using generalized cross-validation [13]. For this model the estimate of the RTOP is a linear function of the coefficients, thus equation (15) applies. We found that the RTOP was on average overestimated. As shown in Figure 2, the size of the bias (difference between average and correct value) depends on both the Rician character of the signal and the maximum b -value used. With the settings used in our simulation (in particular, Rician measurements), the bias is smallest when $b \leq 3000 \text{ s/mm}^2$ and the maximum



Figure 2: Average ratio of estimated to true values of the return to origin probability (RTOP) in 1000 simulated measurements following Gaussian or Rician distributions with scale $\sigma = 0.05S_0$. The signal was generated from a 60° double tensor model and was fitted using anisotropic MAPL models of orders 4, 6 and 8 with regularization strength determined by generalized cross-validation. The experimental parameters were the same as in the Human Connectome Project, except that the maximum b -value, b_{max} , used in the fitting was gradually increased.

order of the MAP-MRI coefficients is 4. Nevertheless — even when using these settings — the bias has an immediate effect on a P-P plot as evident from Figure 3a. We did, however, find that it was possible to remove this confounding effect from the P-P plot by subtracting the bias from the theoretical quantiles before comparing with the correct value, see Figure 3b. This corresponds to shifting the mean of the posterior distribution to the correct value.

Next, we investigated the posterior distribution of the crossing angle when using Constrained Spherical Deconvolution (CSD) [41]. The crossing angle was estimated as the angle between the two largest peaks on the fiber orientation distribution function, provided this angle was at least 25° . We found the peak detection to be more accurate when using only single-shell data. Consequently, we used only the $b = 3000 \text{ s/mm}^2$ shell to fit a CSD model of order 8 with parameters $\lambda = 5$ and $\tau = 0.1$ to each simulated measurement. The single tensor model was used as the response function. In all but 1 case, the peak detection algorithm successfully detected two distinct peaks. The average estimate of the crossing angle was 59.3° . Figure 4 shows the resulting P-P plots before and after correcting for the (small) bias.

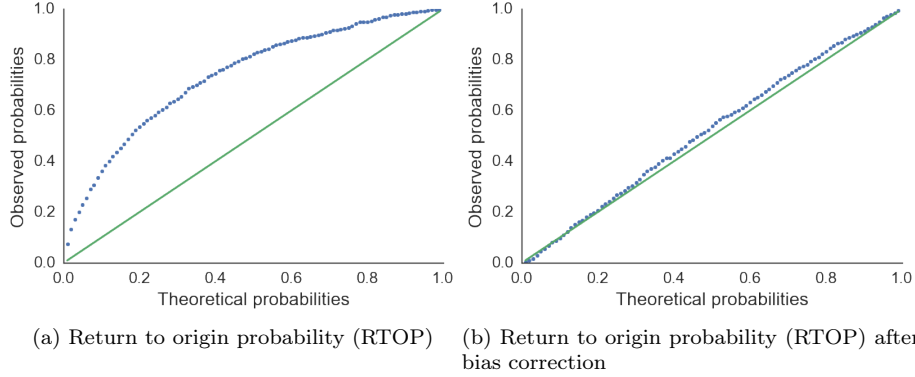


Figure 3: P-P plots of return to origin probability for 1000 simulated measurements from a 60° double tensor model fitted with an anisotropic MAPL model of order 4. Averaging over the simulations, the P-P plots show how often the correct value is smaller than the quantiles corresponding to the theoretically expected probabilities for that property given a simulated measurement. In (b), the bias (average error of the mean) was subtracted from the theoretical quantiles before comparing with the correct value; this corresponds to shifting the mean of the posterior distribution to the correct value.

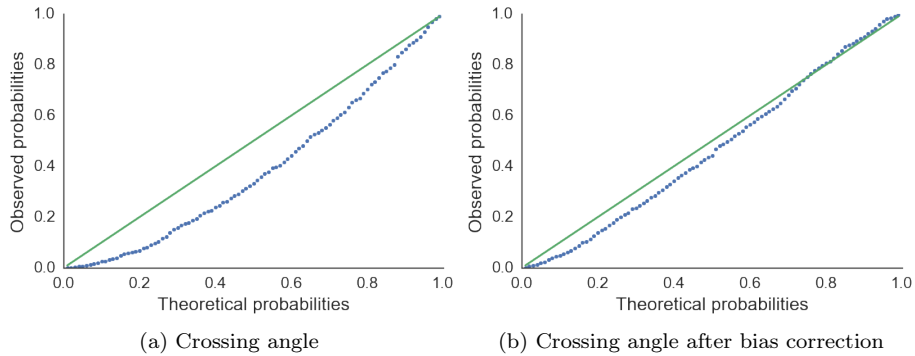


Figure 4: P-P plots of the crossing angle for 1000 simulated measurements from a 60° double tensor model fitted with a constrained spherical deconvolution (CSD) model of order 8. Averaging over the simulations, the P-P plots show how often the correct value is smaller than the quantiles corresponding to the theoretically expected probabilities for that property given a simulated measurement. In (b), the bias (average error of the mean) was subtracted from the theoretical quantiles before comparing with the correct value; this corresponds to shifting the mean of the posterior distribution to the correct value.

3.2 In vivo data

We used the freely available MGH adult diffusion dataset from the Human Connectome Project^{2,3} (HCP) [43]. The subjects are healthy adults, scanned on a customized Siemens 3T Connectome scanner [27, 37] using a Stejskal-Tanner type diffusion weighted spin-echo sequence. The downloaded data have already been corrected for gradient nonlinearities, subject motion and eddy currents [2]. Diffusion measurements were at four b-value shells: 1000, 3000, 5000, 10000 s/mm². The corresponding number of gradient orientations were 64, 64, 128 and 256. A total of 40 non-diffusion weighted ($b = 0$) images were acquired at regular intervals.

We analyzed subjects `mgh_1007` and `mgh_1010`. First, we used the same procedure as in the single tensor simulation to fit a diffusion tensor model (weighted least-squares on $b \leq 1000$ s/mm²). We estimated the posterior distribution of fractional anisotropy in each voxel from a draw of 1000 samples. The mean and the interquartile range of the fractional anisotropy is shown in Figure 5. Second, we used all measurements with $b \leq 3000$ s/mm² to fit an anisotropic MAP-MRI model of order 6 with Laplacian regularization determined by generalized cross validation. Figure 6 shows the mean and interquartile range of the return to origin probability in each voxel. On a standard laptop, the computation time needed to estimate FA by fitting a DTI model to each voxel in a slice, such as in Figure 5, was about 3 s whereas sampling in order to estimate the interquartile range required about 90 s. Similarly, estimating RTOP by fitting a MAP-MRI model required about 220 s whereas obtaining the corresponding, closed-form, estimates of the interquartile range only required 3 s.

4 Discussion

4.1 Interpretation of the results

For the single tensor simulation fitted with DTI, the P-P plots in Figure 1 for mean diffusivity and fractional anisotropy show excellent agreement between theory and observation. This is expected due to the almost perfect match between model and (simulated) measurements — the signal is generated by a DTI model and for $b = 1000$ s/mm² the signal-to-noise ratio is roughly between 5 and 15, meaning that the likelihood (i.e. measurement distribution) is well approximated as Gaussian [19, 36].

We find the P-P plots from the double tensor simulation (Figures 3 and 4) more interesting. It is evident, in particular from Figure 3a, that a P-P plot is only informative if the means of the distributions are approximately equal. After this was addressed by subtracting the bias from the theoretical quantiles, we can see, in Figures 3b and 4b, that there is good agreement between the bias-corrected theoretical distributions and the observed ones. This indicates

²<http://www.humanconnectome.org/documentation/MGH-diffusion/>

³<https://ida.loni.usc.edu/login.jsp>

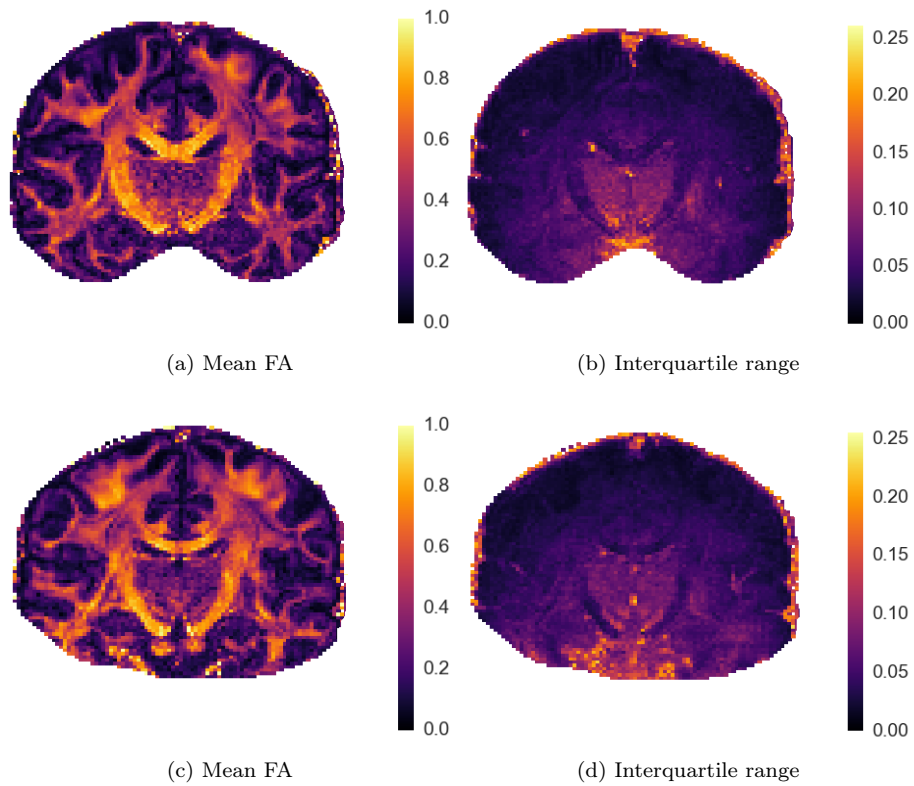


Figure 5: Mean and interquartile range of the fractional anisotropy (FA) estimated using a DTI model fitted with weighted least-squares. The figures correspond to subjects `mgh_1007` (top) and `mgh_1010`(bottom) in the MGH adult diffusion dataset, but using only measurements with $b \leq 1000 \text{ s/mm}^2$

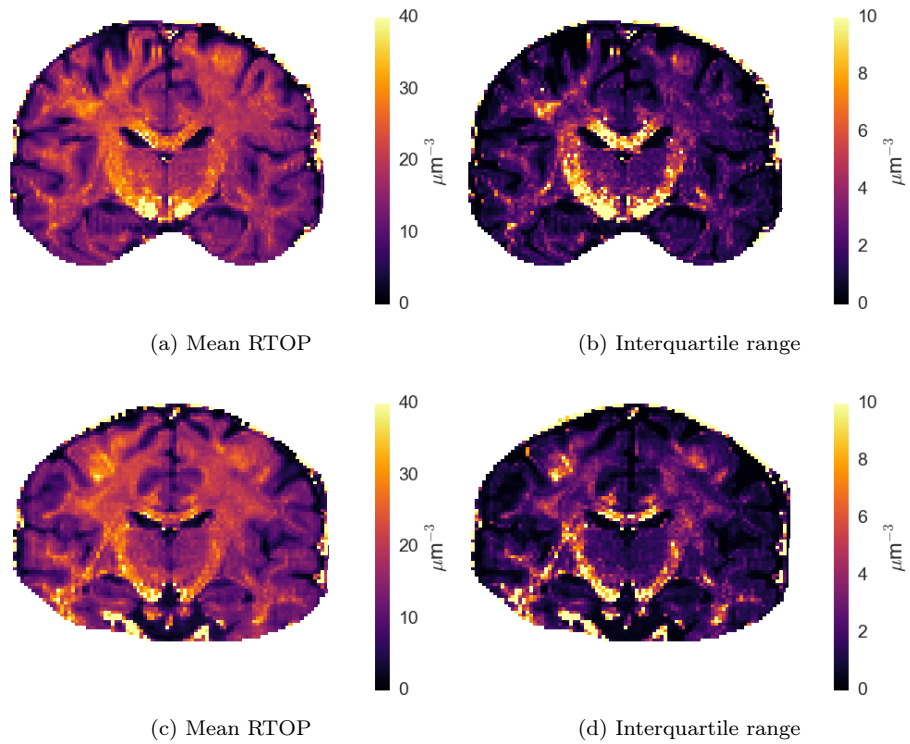


Figure 6: Mean and interquartile range of the return to origin probability (RTOP) estimated using an anisotropic MAP-MRI model of order 6 with Laplacian regularization. The figures correspond to subjects `mgh_1007` (top) and `mgh_1010` (bottom) in the MGH adult diffusion dataset, but using only measurements with $b \leq 3000 \text{ s/mm}^2$.

that the shapes of the posterior distributions are similar to the correct ones, but that their means differ. In other words, the uncertainty quantification is accurate although the point estimate (the mean) is not.

For the scalar indices extracted from in vivo data and shown in Figures 5 and 6, we find that the noise levels that can be appreciated qualitatively from the mean images correspond well with larger interquartile ranges. We note that the FA uncertainty appears to increase with the distance from the head’s surface. For the RTOP uncertainty, on the other hand, the predominant effect seems to be that the uncertainty correlates with the value of the RTOP. In other words, the RTOP estimates appear to be heteroscedastic.

Although we have not made any effort to optimize our implementation for performance, we argue that the additional computational cost of uncertainty quantification is within reason. In particular, if the model is complex and the quantity of interest is an affine function of the coefficients — as was the case with the RTOP estimation using MAP-MRI — then the computational overhead of the uncertainty quantification is almost negligible. The FA estimation using DTI, on the other hand, is an example where fitting the model is cheap but estimating the uncertainty requires sampling. Nevertheless, we believe that the computational overhead incurred by the uncertainty quantification still makes it feasible to use for group analyses.

4.2 General reflections

The class of models fitted with linear least-squares encompasses many of the most popular models. Nevertheless, it would be possible to conduct the same type of probabilistic reasoning for many of the outstanding models, e.g. those using l_1 -penalization (which would correspond to having a Laplace prior on the coefficients). The catch, however, is that it would no longer be possible to arrive at a closed form expression for the posterior distribution. However, it would still be possible to estimate the posterior by Monte Carlo sampling or approximate methods such as variational Bayes [16]. It could then be viewed as part of a general framework called probabilistic programming [17].

In addition to using uncertainty in group analyses and tractography, as we have described before, there are other applications where it could prove useful. One example is in the calculation of the ensemble averaged propagator (EAP), e.g. as proposed in [38].

As an aside, we would like to take the chance to point out the ambiguous use of the term “probabilistic tractography”. In the perhaps most common usage, it refers to the fiber orientation being sampled from a fiber orientation distribution function (fODF). This usage is to contrast it with deterministic tractography, wherein the maximum value of the fODF defines the fiber orientation. The other usage of “probabilistic tractography” refers to probabilistic modeling of the uncertainty in the model, which results in a probability distribution over models. There is thus a hierarchical relationship between the two types of probabilistic tractography, where the latter could perhaps be better described as “meta-probabilistic”. Incidentally, if both types are used simul-

taneously, it results in a compound probability distribution, also known as a mixture distribution [16].

5 Conclusions

We make a Bayesian reinterpretation of some of the most popular algorithms for signal estimation in dMRI. In this interpretation, the commonly used point estimates only constitute the mean of a multivariate probability distribution. With access to this distribution it is, in principle, possible to quantify the uncertainty of any derived quantity. In particular, for quantities that are affine functions of the coefficients the posterior can be expressed in closed-form. Two applications that we think would benefit in particular from this type of uncertainty quantification are dMRI based group analyses and tractography.

Acknowledgements

This study was supported by the Swedish Foundation for Strategic Research grant AM13-0090, the Swedish Research Council CADICS Linneaus research environment, the Swedish Research Council grants 2012-4281, 2013-5229, 2015-05356 and 2016-04482, Linköping University Center for Industrial Information Technology (CENIIT), VINNOVA/ITEA3 BENEFIT grant 2014-00593, and National Institutes of Health grants P41EB015902, R01MH074794, P41EB015898, and the Knut and Alice Wallenberg Foundation project “Seeing Organ Function”.

Data collection and sharing for this project was provided by the Human Connectome Project (HCP; Principal Investigators: Bruce Rosen, M.D., Ph.D., Arthur W. Toga, Ph.D., Van J. Weeden, MD). HCP funding was provided by the National Institute of Dental and Craniofacial Research (NIDCR), the National Institute of Mental Health (NIMH), and the National Institute of Neurological Disorders and Stroke (NINDS). HCP data are disseminated by the Laboratory of Neuro Imaging at the University of Southern California.

Conflict of interest statement

Declarations of interest: none.

A Marginalization over the residual variance

In this section we first show that by placing an inverse-Gamma prior over the residual variance σ^2 , the posterior becomes a multivariate t -distribution. Then we show that it is possible to choose the prior hyperparameters such that the covariance and the degrees of freedom remain the same as before putting a prior over σ^2 , ultimately leading to the expressions in equations (13) and (14).

The inverse-Gamma distribution is a convenient choice because it is the conjugate prior for σ^2 . Its probability distribution is

$$p(\sigma^2) = IG(\alpha, \beta) = \frac{\beta^\alpha}{\Gamma(\alpha)} \frac{1}{(\sigma^2)^{\alpha+1}} \exp\left(-\frac{\beta}{\sigma^2}\right), \quad (22)$$

where $\Gamma(\cdot)$ is the Gamma function.

The joint posterior of \mathbf{c} and σ^2 can be computed by combining the Gaussian likelihood (5), the Gaussian prior (6) on the coefficients and the Inverse-Gamma prior (22) on σ^2 ,

$$\begin{aligned} p(\mathbf{c}, \sigma^2 | \mathbf{y}, \mathbf{x}) &\propto p(\mathbf{y} | \mathbf{c}, \sigma^2, \mathbf{x}) p(\mathbf{c} | \sigma^2) p(\sigma^2) \\ &= \frac{|W|^{1/2}}{(2\pi\sigma^2)^{n/2}} \exp\left(-\frac{1}{2\sigma^2} (\mathbf{y} - \Phi\mathbf{c})^T W (\mathbf{y} - \Phi\mathbf{c})\right) \\ &\cdot \frac{|\Lambda|^{1/2}}{(2\pi\sigma^2)^{d/2}} \exp\left(-\frac{1}{2\sigma^2} \mathbf{c}^T \Lambda \mathbf{c}\right) \cdot \frac{\beta^\alpha}{\Gamma(\alpha)} \frac{1}{(\sigma^2)^{\alpha+1}} \exp\left(-\frac{\beta}{\sigma^2}\right) \\ &\propto (\sigma^2)^{-(\alpha+1+\frac{n}{2}+\frac{d}{2})} \exp\left(-\frac{1}{\sigma^2} \left(\beta + \frac{1}{2} \mathbf{y}^T W \mathbf{y} + \frac{1}{2} (\mathbf{c}^T Q \mathbf{c} - 2\mathbf{c}^T \Phi^T W \mathbf{y})\right)\right) \\ &= (\sigma^2)^{-(\alpha+1+\frac{n}{2}+\frac{d}{2})} \exp\left(-\frac{1}{\sigma^2} \left(\beta + \frac{1}{2} (\mathbf{y}^T W \mathbf{y} - \mathbf{y}^T W \Phi Q^{-1} \Phi^T W \mathbf{y})\right)\right) \\ &\cdot \exp\left(-\frac{1}{2\sigma^2} (\mathbf{c} - Q^{-1} \Phi^T W \mathbf{y})^T Q (\mathbf{c} - Q^{-1} \Phi^T W \mathbf{y})\right) \\ &= \mathcal{N}(\mathbf{c} | \boldsymbol{\mu}, \sigma^2 Q^{-1}) IG(\sigma^2 | \alpha_*, \beta_*), \end{aligned}$$

where

$$\alpha_* = \alpha + \frac{n}{2}, \quad (23)$$

$$\beta_* = \beta + \frac{1}{2} \mathbf{y}^T W (\mathbf{y} - \Phi \boldsymbol{\mu}). \quad (24)$$

Now, we obtain the marginal posterior distribution by integrating over σ^2 ,

$$p(\mathbf{c} | \mathbf{y}, \mathbf{x}) = \int p(\mathbf{c}, \sigma^2 | \mathbf{y}, \mathbf{x}) d(\sigma^2) \quad (25)$$

$$= \int \mathcal{N}(\mathbf{c} | \boldsymbol{\mu}, \Sigma) IG(\sigma^2 | \alpha_*, \beta_*) d(\sigma^2) \quad (26)$$

$$= \frac{\Gamma(\alpha_* + \frac{d}{2})}{\Gamma(\alpha_*)} \frac{|Q|^{1/2}}{(2\pi\beta_*)^{d/2}} \left(1 + \frac{(\mathbf{c} - \boldsymbol{\mu})^T Q (\mathbf{c} - \boldsymbol{\mu})}{2\beta_*}\right)^{-(\alpha_* + \frac{d}{2})} \quad (27)$$

which is in fact a multivariate t -distribution [29, 35] with degrees of freedom $\nu = 2\alpha_*$, mean vector $\boldsymbol{\mu}$ and correlation matrix $R = (\beta_*/\alpha_*)Q^{-1}$. For this result to be usable we must specify the prior hyperparameters α and β . In the spirit of what is commonly referred to as empirical Bayes, we determine these hyperparameters by requiring that the covariance and the degrees of freedom in equation (13) remain the same as before putting a distribution over σ^2 .

Starting from $\nu = 2\alpha_*$, we find by comparing equations (10) and (23) that

$$\alpha = -\frac{1}{2} \text{Tr} \left(2\tilde{H} - \tilde{H}^T \tilde{H} \right). \quad (28)$$

The covariance in (13) is

$$\frac{\nu}{\nu - 2} R = \frac{\beta_*}{\alpha_* - 1} Q^{-1} = E[\sigma^2] Q^{-1}. \quad (29)$$

To get correspondence with the covariance in equation (8), we require that $E[\sigma^2] = \hat{\sigma}^2$. Combining this with equations (24) and (28) gives

$$\beta = -\frac{1}{2} \left(\frac{1}{\alpha_*} \mathbf{y} + \frac{\alpha_* - 1}{\alpha_*} \hat{\mathbf{y}} \right)^T W(\mathbf{y} - \hat{\mathbf{y}}). \quad (30)$$

This means that we can express the degrees of freedom and correlation matrix of the multivariate t -distribution in terms of ν and $\hat{\sigma}^2$ as

$$\begin{aligned} \nu &= \|I - H\|_{\text{Fro}}^2, \\ R &= \frac{\nu - 2}{\nu} \hat{\sigma}^2 Q^{-1}. \end{aligned} \quad (31)$$

References

- [1] J. L. Andersson and S. N. Sotiropoulos. Non-parametric representation and prediction of single-and multi-shell diffusion-weighted MRI data using Gaussian processes. *NeuroImage*, 122:166–176, 2015.
- [2] J. L. Andersson and S. N. Sotiropoulos. An integrated approach to correction for off-resonance effects and subject movement in diffusion MR imaging. *Neuroimage*, 125:1063–1078, 2016.
- [3] H.-E. Assemlal, D. Tschumperlé, and L. Brun. Efficient and robust computation of PDF features from diffusion MR signal. *Medical image analysis*, 13(5):715–729, 2009.
- [4] P. J. Basser, J. Mattiello, and D. LeBihan. MR diffusion tensor spectroscopy and imaging. *Biophysical journal*, 66(1):259, 1994.
- [5] T. E. Behrens, H. J. Berg, S. Jbabdi, M. F. Rushworth, and M. W. Woolrich. Probabilistic diffusion tractography with multiple fibre orientations: What can we gain? *Neuroimage*, 34(1):144–155, 2007.
- [6] T. E. Behrens, M. W. Woolrich, M. Jenkinson, H. Johansen-Berg, R. G. Nunes, S. Clare, P. M. Matthews, J. M. Brady, and S. M. Smith. Characterization and propagation of uncertainty in diffusion-weighted MR imaging. *Magnetic resonance in medicine*, 50(5):1077–1088, 2003.
- [7] C. M. Bishop. *Pattern recognition and machine learning*. Springer, 2006.

- [8] E. Caruyer and R. Deriche. Diffusion MRI signal reconstruction with continuity constraint and optimal regularization. *Medical image analysis*, 16(6):1113–1120, 2012.
- [9] G. Chen, Z. S. Saad, A. R. Nath, M. S. Beauchamp, and R. W. Cox. FMRI group analysis combining effect estimates and their variances. *Neuroimage*, 60(1):747–765, 2012.
- [10] S. Chung, Y. Lu, and R. G. Henry. Comparison of bootstrap approaches for estimation of uncertainties of DTI parameters. *NeuroImage*, 33(2):531–541, 2006.
- [11] M. Descoteaux, E. Angelino, S. Fitzgibbons, and R. Deriche. Apparent diffusion coefficients from high angular resolution diffusion imaging: Estimation and applications. *Magnetic Resonance in Medicine*, 56(2):395–410, 2006.
- [12] M. Descoteaux, E. Angelino, S. Fitzgibbons, and R. Deriche. Regularized, fast, and robust analytical Q-ball imaging. *Magnetic resonance in medicine*, 58(3):497–510, 2007.
- [13] R. H. Fick, D. Wassermann, E. Caruyer, and R. Deriche. MAPL: Tissue microstructure estimation using Laplacian-regularized MAP-MRI and its application to HCP data. *NeuroImage*, 134:365–385, 2016.
- [14] J. Friedman, T. Hastie, and R. Tibshirani. *The elements of statistical learning*, volume 1. Springer series in statistics New York, 2001.
- [15] E. Garyfallidis, M. Brett, B. Amirbekian, A. Rokem, S. Van Der Walt, M. Descoteaux, I. Nimmo-Smith, and D. Contributors. Dipy, a library for the analysis of diffusion MRI data. *Frontiers in neuroinformatics*, 8, 2014.
- [16] A. Gelman, J. B. Carlin, H. S. Stern, D. B. Dunson, A. Vehtari, and D. B. Rubin. *Bayesian Data Analysis*. CRC Press, 2013.
- [17] Z. Ghahramani. Probabilistic machine learning and artificial intelligence. *Nature*, 521(7553):452, 2015.
- [18] X. Gu, P. Sidén, B. Wegmann, A. Eklund, M. Villani, and H. Knutsson. Bayesian diffusion tensor estimation with spatial priors. In *International Conference on Computer Analysis of Images and Patterns*, pages 372–383. Springer, Cham, 2017.
- [19] H. Gudbjartsson and S. Patz. The Rician distribution of noisy MRI data. *Magnetic resonance in medicine*, 34(6):910–914, 1995.
- [20] H. A. Haroon, D. M. Morris, K. V. Embleton, D. C. Alexander, and G. J. Parker. Using the model-based residual bootstrap to quantify uncertainty in fiber orientations from q -ball analysis. *IEEE transactions on medical imaging*, 28(4):535–550, 2009.

- [21] C. P. Hess, P. Mukherjee, E. T. Han, D. Xu, and D. B. Vigneron. Q-ball reconstruction of multimodal fiber orientations using the spherical harmonic basis. *Magnetic Resonance in Medicine*, 56(1):104–117, 2006.
- [22] J. H. Jensen, J. A. Helpert, A. Ramani, H. Lu, and K. Kaczynski. Diffusional kurtosis imaging: The quantification of non-Gaussian water diffusion by means of magnetic resonance imaging. *Magnetic resonance in medicine*, 53(6):1432–1440, 2005.
- [23] B. Jeurissen, A. Leemans, D. K. Jones, J.-D. Tournier, and J. Sijbers. Probabilistic fiber tracking using the residual bootstrap with constrained spherical deconvolution. *Human brain mapping*, 32(3):461–479, 2011.
- [24] H. Johansen-Berg and M. F. Rushworth. Using diffusion imaging to study human connective anatomy. *Annual review of neuroscience*, 32:75–94, 2009.
- [25] D. K. Jones. Determining and visualizing uncertainty in estimates of fiber orientation from diffusion tensor MRI. *Magnetic Resonance in Medicine*, 49(1):7–12, 2003.
- [26] D. K. Jones. Tractography gone wild: probabilistic fibre tracking using the wild bootstrap with diffusion tensor MRI. *IEEE transactions on medical imaging*, 27(9):1268–1274, 2008.
- [27] B. Keil, J. N. Blau, S. Biber, P. Hoecht, V. Tountcheva, K. Setsompop, C. Triantafyllou, and L. L. Wald. A 64-channel 3T array coil for accelerated brain MRI. *Magnetic resonance in medicine*, 70(1):248–258, 2013.
- [28] C. G. Koay, L.-C. Chang, C. Pierpaoli, and P. J. Basser. Error propagation framework for diffusion tensor imaging via diffusion tensor representations. *IEEE transactions on medical imaging*, 26(8):1017–1034, 2007.
- [29] S. Kotz and S. Nadarajah. *Multivariate t-distributions and their applications*. Cambridge University Press, 2004.
- [30] C. Loader. *Local regression and likelihood*. Springer-Verlag New York, 1999.
- [31] E. Özarslan, C. Koay, T. Shepherd, M. Komlosh, M. İrfanoğlu, C. Pierpaoli, and P. Basser. Mean apparent propagator (MAP) MRI: a novel diffusion imaging method for mapping tissue microstructure. *NeuroImage*, 78:16–32, 2013.
- [32] E. Özarslan, B. C. Vemuri, and T. H. Mareci. Generalized scalar measures for diffusion MRI using trace, variance, and entropy. *Magnetic resonance in Medicine*, 53(4):866–876, 2005.
- [33] C. Pierpaoli and P. J. Basser. Toward a quantitative assessment of diffusion anisotropy. *Magnetic resonance in Medicine*, 36(6):893–906, 1996.

- [34] J. O. Rawlings, S. G. Pantula, and D. A. Dickey. *Applied regression analysis: a research tool*. Springer Science & Business Media, 2001.
- [35] M. Roth. On the multivariate t distribution. Technical report, Linköping University, Department of Electrical Engineering, 2012.
- [36] R. Salvador, A. Peña, D. K. Menon, T. A. Carpenter, J. D. Pickard, and E. T. Bullmore. Formal characterization and extension of the linearized diffusion tensor model. *Human brain mapping*, 24 2:144–55, 2005.
- [37] K. Setsompop et al. Pushing the limits of in vivo diffusion MRI for the Human Connectome Project. *Neuroimage*, 80:220–233, 2013.
- [38] J. Sjölund, A. Eklund, E. Özarslan, and H. Knutsson. Gaussian process regression can turn non-uniform and undersampled diffusion MRI data into diffusion spectrum imaging. In *IEEE 14th International Symposium on Biomedical Imaging (ISBI)*, pages 778–782. IEEE, 2017.
- [39] S. M. Smith, M. Jenkinson, H. Johansen-Berg, D. Rueckert, T. E. Nichols, C. E. Mackay, K. E. Watkins, O. Ciccarelli, M. Z. Cader, P. M. Matthews, et al. Tract-based spatial statistics: voxelwise analysis of multi-subject diffusion data. *Neuroimage*, 31(4):1487–1505, 2006.
- [40] E. Stejskal and J. Tanner. Spin diffusion measurements: spin echoes in the presence of a time-dependent field gradient. *The journal of chemical physics*, 42(1):288–292, 1965.
- [41] J.-D. Tournier, F. Calamante, and A. Connelly. Robust determination of the fibre orientation distribution in diffusion MRI: non-negativity constrained super-resolved spherical deconvolution. *Neuroimage*, 35(4):1459–1472, 2007.
- [42] D. S. Tuch. Q-ball imaging. *Magnetic resonance in medicine*, 52(6):1358–1372, 2004.
- [43] D. Van Essen, S. Smith, D. Barch, T. Behrens, E. Yacoub, and K. Ugurbil. The WU-Minn Human Connectome Project: an overview. *Neuroimage*, 80:62–79, 2013.
- [44] J. Veraart, J. Sijbers, S. Sunaert, A. Leemans, and B. Jeurissen. Weighted linear least squares estimation of diffusion MRI parameters: strengths, limitations, and pitfalls. *NeuroImage*, 81:335–346, 2013.
- [45] B. Wegmann, A. Eklund, and M. Villani. Bayesian Rician regression for neuroimaging. *Frontiers in Neuroscience*, 11:586, 2017.
- [46] C. F. Westin, H. Knutsson, O. Pasternak, F. Szczepankiewicz, E. Özarslan, D. van Westen, C. Mattisson, M. Bogren, L. J. O’Donnell, M. Kubicki, et al. Q-space trajectory imaging for multidimensional diffusion MRI of the human brain. *Neuroimage*, 135:345–362, 2016.

- [47] B. Whitcher, D. S. Tuch, J. J. Wisco, A. G. Sorensen, and L. Wang. Using the wild bootstrap to quantify uncertainty in diffusion tensor imaging. *Human brain mapping*, 29(3):346–362, 2008.
- [48] M. B. Wilk and R. Gnanadesikan. Probability plotting methods for the analysis of data. *Biometrika*, 55(1):1–17, 1968.
- [49] M. W. Woolrich, T. E. Behrens, C. F. Beckmann, M. Jenkinson, and S. M. Smith. Multilevel linear modelling for fMRI group analysis using Bayesian inference. *Neuroimage*, 21(4):1732–1747, 2004.
- [50] Y. Yuan, H. Zhu, J. G. Ibrahim, W. Lin, and B. S. Peterson. A note on the validity of statistical bootstrapping for estimating the uncertainty of tensor parameters in diffusion tensor images. *IEEE transactions on medical imaging*, 27(10):1506–1514, 2008.